



## Scientific - Research Article

# A Method for Selection of Optimum Solidity in the Design of a Tandem Compressor Blade Row

Hamzeh Eshraghi<sup>1</sup>

1-Department of Aerospace Engineering, Amirkabir University of Technology, Tehran, Iran

### ABSTRACT

**Keywords:** Optimum, Solidity, Tandem, Compressor

*In the current article, using the results of previous researches, a guideline has been developed to select a proper value for the solidity of a tandem blade row in an axial flow compressor stage. Next, a highly loaded tandem compressor stage has been designed using this guideline. Some other cases have been designed with different solidity values to verify the selected solidity value. Other geometrical parameters have been selected similarly in all cases. At the next stage, a three-dimensional numerical model is developed to predict the characteristic performance of each tandem stage. The model is validated with the experimental results of NASA Stage and Rotor 37, and the model's accuracy level is presented. Using a similar model, the performance of all cases has been derived, and the effect of solidity variation on the machine's overall performance has been discussed. Lastly, the effect of solidity variation on the tip leakage flow structure near the peak efficiency point is discussed for all cases.*

### Nomenclature

AO = Axial overlap  
DCA = Double circular arc  
DF = Lieblein diffusion factor  
C = Absolute velocity  
N = Number of blades  
S = Blade-to-blade pitch  
W = Relative velocity  
b = Axial chord  
l = Blade chord length (cm)  
n = Rotational speed (RPM)  
r = Radius (cm)  
t = Pitch-wise distance of tandem blades  
u = Blade velocity  
Greek symbols  
 $\pi$  = Stage total to total pressure ratio  
 $\eta$  = Stage isentropic total to total efficiency  
 $\psi$  = Work coefficient, Rotor total enthalpy rise over the blade velocity square

$\varphi$  = Flow coefficient, Flow axial velocity over the blade velocity  
 $\Lambda$  = Reaction degree, Rotor static enthalpy rise over the stage static enthalpy rise  
 $\alpha$  = Absolute flow angle  
 $\beta$  = Relative flow angle  
 $\xi$  = Blade stagger angle  
 $\sigma$  = Solidity  
 $\theta$  = Tangential velocity component  
Subscripts  
a = Aft blade  
d = Design value  
eff = Effective value  
f = Front blade  
h = Hub value  
m = Mid-height value  
r = Rotor  
s = Stator  
t = Tip value

<sup>1</sup> PhD. (Corresponding Author) Email: \* eshraghi@aut.ac.ir

DOI: [10.22034/jast.2023.365224.1133](https://doi.org/10.22034/jast.2023.365224.1133)

Submit: 10-10-2022 / Accepted: 05/03/2023

Print ISSN:1735-2134 Online ISSN: 2345-3648

## Introduction

Tandem airfoil configuration is a passive boundary layer control method that helps prevent boundary layer separation on the suction surface caused by the positive imposed pressure gradient. This method is based on using two blades instead of one and suggests using the pressure side momentum of the front blade flow to avoid the separation on the aft blade suction side; this ultimately helps achieve higher flow deflection and enables more significant aerodynamic loading and higher work coefficients.

In the past 40 years, several experimental investigations and numerical studies have been performed on tandem blades considering both subsonic and transonic flow regimes. Cheatham [1], and Brent & Clemmons [2] designed and tested a tandem blade compressor stage named stage E. The flow properties were measured, and compressor characteristic maps were reported for uniform and distorted inlet flow. They also performed a similar study on a conventional compressor stage named stage D in which the performance of the conventional compressor stage was reported for both uniform and distorted inlet flow. Both stages were designed for equal rotational speeds, equal hub and shroud geometry, similar effective chord length and equivalent design diffusion factor (DF) value. They concluded that the tandem stage achieves a higher pressure ratio at all rotational speeds. However, for lower rotational speeds, the efficiency of the tandem system was lower than the conventional one. At 100% and 110% of the rotational speed, the tandem design's efficiency was higher than the conventional stage. Bammert & Beelte [3] designed and tested a four-stage compressor with a high degree of reaction. The first stage rotor and all stator rows were designed as single conventional blades, but all other rotor blades used a tandem configuration. In this system, the stagger angle of the stator rows could be varied in order to evaluate the effect of variation of this parameter on the compressor map. Changing the stagger angle resulted in a shift in compressor characteristic maps, a change of characteristic curve slopes, and the surge margin. McGlumphy et al. [4, 5] developed a 2D method for designing tandem cascades based on prescribing specific diffusion factors and the solidity of the tandem cascade.

Employing different geometrical parameters and using CFD models, they offered optimum

geometrical parameters, providing the minimum loss conditions. Using the results of this optimum design of 2D blades, they reported the performance of a high hub/tip ratio subsonic tandem rotor in the 3D frame. It was suggested that using tandem blades in the rear stages of axial flow compressors provides specific advantages to achieve high DF values for blade aerodynamic loading and low loss coefficients. Qiushi et al. [6] carried out a numerical investigation on a tandem stator with supersonic inlet flow. Geometrical parameters were changed, and the optimum values in each case were reported to achieve the minimum loss status. Shen et al. [7] used DCA profile blades in their numerical and experimental study of a tandem cascade. They studied the effect of geometrical configurations on the loss coefficient of the tandem cascade. They also studied the effect of injected flow on the wake formed at the rear side of the blades. Eshraghi et al. [8] developed a methodology in the 3D design of highly loaded tandem axial flow compressor stages based on redefining the non-dimensional cascade performance parameters. They showed that using this procedure makes it possible to achieve high work coefficient values of 0.8, with one tandem rotor. They also designed a single-blade compressor stage with a conventional work coefficient of 0.49 and compared the overall performance of these two compressor stages. In this comparison, first, they showed that the slope of work coefficient vs. flow coefficient ( $\psi$ - $\phi$ ) and pressure ratio ( $\pi$ ) vs. mass flow curves are much lower than the conventional mutual values due to the unique loading parameters. This means that  $\psi$  and  $\pi$  are approximately independent of  $\phi$  or mass flow rates, especially at lower rotational speeds. They also showed that because of more stagnation points, more complicated boundary layer flows and higher sonic regime losses, the efficiency of the tandem design was approximately 3% less than the conventional case.

On the other hand, at its design speed, the tandem case shows about 10% and 48% improvements in  $\pi$  and mass flow rates, respectively. It must be noted that both cases were designed with similar geometrical parameters, the same frontal area, axial width, blade families, and the same rotational speed. They also concluded that using more developed airfoil families may improve the performance of the tandem design.

Mohsen et al. designed a tandem rotor based on NASA 37 rotor **Error! Reference source not**

**found..** It tried to find appropriate values of geometric parameters of the designed blade. A numerical model has been used for performance evaluation, and the numerical results reveal that significant improvements in flow turning and diffusion are obtained without flow separation. The tandem design has a 17% increase in the total pressure ratio and a 2% increase in the rotor's adiabatic efficiency compared to the original NASA Rotor 37.

Shaoyuan et al. using an optimization algorithm, redesigned a stator row for NASA 35 compressor stage [10]. The geometric parameters of the tandem stator have been optimized. The compressor stage's performance and flow field have been derived using a numerical CFD method. Compared to the original NASA 35 stator, the optimized tandem stator could archive more turning angle of 28°.

Song et al. developed an optimization method to design a tandem 2D cascade and validated the presented method using numerical CFD investigation [11]. The optimization goal of total pressure loss has been selected, and they showed that the total pressure loss had decreased by more than 50% using the presented method. They also concluded that the multi-objective optimization for 3D blades must be conducted.

Yang et al. performed a numerical investigation on a tandem 2D cascade [12]. They studied the effects of off-design incidence angles and the inlet boundary layer thickness on the total pressure loss of the compressor cascade. They concluded that the inlet boundary layer thickness reduces the tandem cascade performance advantage. Also, they declared that more attempts are needed to address the cascade results through the 3D twisted blades and end-wall flow characteristics.

Many parameters in the tandem concept affect the overall system performance. Some of the mentioned studies give helpful guidelines for designing a proper tandem configuration. For example, the relative orientation of front and aft blades has been deeply studied, and the optimum values of these geometrical parameters have been reported. However, there is still room to investigate other influential parameters such as rotor-stator axial width, radius ratio, tip clearance or blade solidity.

The current study suggests a guideline to select the proper value for solidity in a tandem design. Then a highly loaded tandem stage is designed using the suggested procedure. To investigate the effect of

solidity variation on the performance of this designed case, other cases with different values of solidity are designed and analyzed numerically. Furthermore, the optimum solidity value and the effect of solidity variation on the overall performance and tip leakage flow structure will be investigated.

### Geometrical presentation of a tandem cascade

Geometrical parameters, which are needed to describe a tandem cascade, are depicted in Fig. 1. Chord length ( $l$ ) and stagger angle ( $\xi$ ) are defined for both front and aft blades. Subsequently, the effective values of these parameters are also introduced for a tandem blade set. Likewise, the axial overlap of tandem blades (AO) is presented.

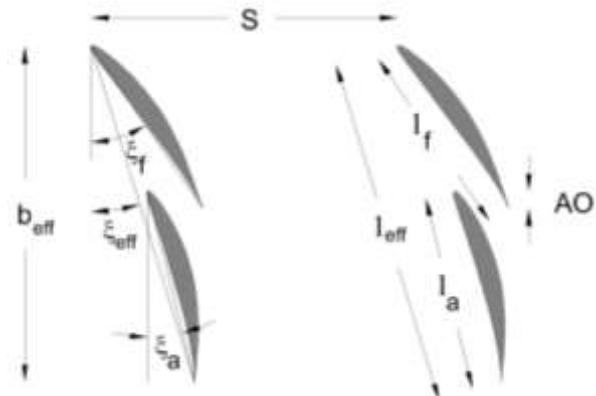


**Fig. 1.** Geometrical parameterization for tandem cascade

In the current study, regarding the recent geometric parameterization, the effective solidity is defined as a function of front and aft solidities, axial overlap percentage, and front, aft and effective stagger angles of the cascade as follows. Axial overlap percent, %AO, and Pitch percent (%P) are defined as below:

$$\%P = \frac{t}{S} \quad (1)$$

$$\%AO = \frac{AO}{b_{eff}} \quad (2)$$

Where  $b_{eff}$  is the effective axial chord and is defined by equation 3 as below:

$$b_{eff} = (l_f \cdot \cos \xi_f + l_a \cdot \cos \xi_a - AO) \quad (3)$$

Then, effective chord and effective solidity will be defined respectively by equations 4 and 5:

$$l_{eff} = \frac{b_{eff}}{\cos \xi_{eff}} \quad (4)$$

$$\begin{aligned} \sigma_{\text{eff}} &= \frac{C_{\text{eff}}}{S} \quad (5) \\ &= \frac{1}{\cos \xi_{\text{eff}}} \left( (\sigma_f \cos \xi_f \right. \\ &\quad \left. + \sigma_a \cos \xi_a) - \frac{AO}{S} \right) \end{aligned}$$

In the present study, this definition of solidity not only uses the effect of %AO but it also considers the effect of stagger angle redundancy.

### Solidity selection strategy

There are many numerical and experimental investigations which have resulted in correlations that guide the selection of the optimum value of solidity for a single-blade configuration. In this study, the results of Tournier & El-Genk [13] are used which are based on the inlet and the outlet flow angles and also on minimizing the summation of profile and secondary loss coefficients.

However, the first question here is how to select a proper value for the solidity of a tandem configuration which has two blades instead of one in each passage. In a series of 2D numerical analyses, McGlumphy et al. [4] concluded that the front blade in a tandem cascade behaves as an individual blade, but the aft blade's behavior strongly depends on the front blade's flow characteristics. Considering this statement, the solidity value for the front blade is optimized here, followed by the calculation of the optimal number of front blades. It must be noted that the number of front and aft blades must be equal for either the rotor or the stator rows; otherwise, the %P value will be changed in the circumferential direction. Since the number of aft blades is set, the aft blade's chord length must be changed to optimize the solidity of these blades.

To find the front blade's optimal solidity, the general form of the tandem cascade velocity triangles, which was also used in [8] must be presented. It is demonstrated in Fig. 2.

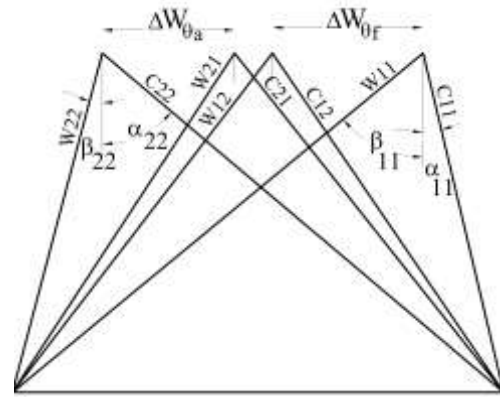


Fig. 2. General velocity triangles of a tandem stage

The velocity triangles are presented for a repeatable case to ease the presentation. In this case, the flow enters into the rotor front blades with a relative velocity of  $W_{11}$  and leaves them with  $W_{12}$ . The relative velocity at the entry to the aft blade is  $W_{21}$  while it leaves the rotor row with  $W_{22}$ . The front blades of the stator receive the flow with the absolute velocity of  $C_{22}$  and the exit velocity of  $C_{21}$  at the trailing edge. Similarly, the flow enters the aft blades of the stator with  $C_{12}$  and leaves there with  $C_{11}$ . Respective velocity vectors are indicated in Fig. 3.



Fig. 3. Velocity vectors in a tandem stage

Considering what was mentioned above and also to optimize the solidity of the rotor's front blade, it is necessary to use  $\beta_{11}$  and  $\beta_{12}$  angles. To find the stator front blade solidity value, it is also needed to use  $\alpha_{22}$  and  $\alpha_{21}$ . McGlumphy et al. [4] suggest using an equal value for  $\beta_{12}$  and  $\beta_{21}$ . This assumption simplifies the general velocity triangles, as demonstrated in Fig. 4, and can be used for both rotor and stator blade rows.

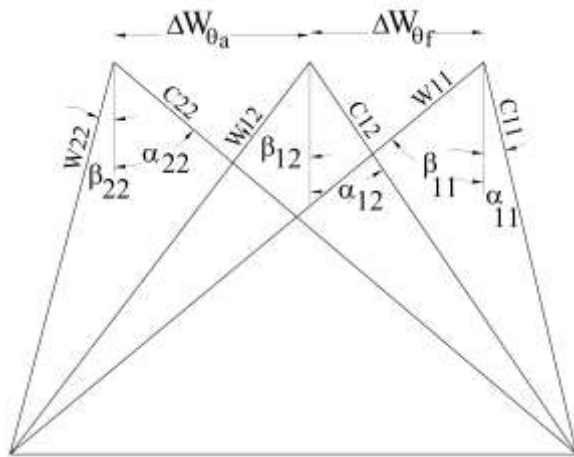


Fig. 4. Simplified tandem velocity triangles

This assumption has been checked and verified in some 2D and 3D cases reported by McGlumphy et al. [4, 5] and Eshraghi et al.[8]. It has also been used in the current study. In a 3D case, velocity triangles change from hub to tip due to the applied swirl distribution. Because of the blade’s twist, the optimal solidity may vary with changing radius. It is possible to set the optimal solidity at the mid-height radius and change the chord length from hub to tip. Using this strategy, the solidity may be in its optimal aerodynamic condition. However, to ensure the mechanical behavior of the blade against the aerodynamic loads, a Fluid-Structure Interaction investigation must be performed. As another solution, the solidity value may be optimized for the blade mid-height radius, and then the number of blades would be derived. Using the constant chord length for the whole blade may result in the solidity deviation from its optimal values in different radii. Still, it ensures the blade’s strength against aerodynamic loads. In this investigation, the second solution has been used.

**Design specifications**

The current tandem compressor stage has been designed using the design procedure developed and published by Eshraghi et al.[8]. This methodology is based on redefining the non-dimensional cascade performance parameters. It was shown that using the tandem concept can increase the  $\psi$  values as high as 0.8, without a significant efficiency drop.

The current tandem compressor stage is designed to receive an axial flow with zero swirls at the inlet ( $\alpha_{11}$  is set to zero) using repeatable velocity triangles (stage inlet and outlet absolute flow angles are equal). Design specifications for the

reference condition are presented in Table 1. Non-dimensional parameters are reported for blade mid-height radius.

**Table 1.** Design specifications for the designed tandem stage.

Parameter	Value
$n_d$ (RPM)	3300
$\psi$	0.86
$\phi$	0.89
$\Lambda$	0.57
$r_h$ (cm)	40
$r_t$ (cm)	50
$l^I$ (cm)	4
% $AO_m$ r,s	5, 5
% $P_m$ r,s	75, 80
$N^{II}$	64
Tip Clearance (mm)	2.00

Note I: Reported chord length had been set for each individual blade.

Note II: Numbers of blades indicate the number of pair sets for tandem rotor and stator rows.

Using described  $\psi$ ,  $\phi$  and  $\Lambda$  values in Table 1, results in the following flow angles in the blade mid-height radius in Table 2.

**Table 2.** Mid-Span flow angles through the tandem stage

	$\beta_{11}$	$\beta_{12}$	$\beta_{22}$
<b>Rotor flow angles (degrees)</b>	48.33	32.64	8.94
	$\alpha_{22}$	$\alpha_{12}$	$\alpha_{11}$
<b>Stator flow angles (degrees)</b>	44.00	25.79	00.00

Using the described strategy in part III, the optimal solidity for the rotor and stator front blades will be 0.9 and 0.95, respectively. Likewise, the optimal solidity of aft blades will be 1.00 for both rotor and stator rows. In order to find an integer value for the number of blades, it is decided to set the solidity as 0.905 for both rotor and stator, front and aft blades. Therefore, the reference case would have 64 blades. In order to investigate the effect of solidity on the performance of the tandem design, other cases have been designed and analyzed with exactly the same design characteristics but different solidity values. The range of this variation is tabulated in Table 3 as follows.

**Table 3.** Solidity deviations from the reference case and the respective number of blades

$\Delta\sigma$ from ref. value	Solidity ( $\sigma$ )	Number of Blades
-21%	0.715	50
-11%	0.805	57
0.0%	0.905	64
+11%	1.005	71
+22%	1.104	78
+32%	1.195	85
+44%	1.303	92
+55%	1.403	99

A partial view of the reference case is depicted in Fig. 5



**Fig. 5.** 3D View of the reference case

In all cases, blade profiles are stacked on the centroid of the profile and the stacking line is selected to be a straight line perpendicular to the machine axis. The blade family of NACA65 with a maximum thickness/chord ratio of 10%, is used for all airfoils.

### Numerical methodology

To study the flow field and analyze the overall performance, a 3D numerical analysis has been performed with the commercial CFD code, CFX-5. CFX solves the steady and unsteady, compressible and incompressible Reynolds-averaged, Navier-Stokes (RANS) equations using the finite volume approach. CFX uses a cell-vertex approach for domain discretization; Primitive variables, velocity vector components, pressure and temperature values etc., are stored on the corner of elements. RANS Equations are integrated on control volumes, and Gauss's theorem is used to exchange the volumetric integrals into surface integrals. Then a set of algebraic equations is generated to solve the values of pressure and velocity vectors.

The following boundary conditions are used for all 3D flow simulations in this study:

Total pressure and temperature, flow direction and turbulent intensity for stage inlet are set to be 1atm, 288K, axial direction and 5%, respectively

Smooth wall for blades, hubs and shrouds

Average static pressure in stage outlet (starting from 1atm)

A single passage is modelled for rotor and stator rows, so periodic rotational interfaces are used for the side boundaries of the passage block. To obtain the performance characteristic of the compressor stage, outlet pressure has been increased gradually until numerical instability is observed. Convergence criteria are set to be  $10^{-5}$  for RMS residual. Pressure ratio and total to total efficiency values are derived from the mass flow averaging procedure from inlet and outlet flow conditions. For turbulence modelling, the k- $\epsilon$  model with scalable wall function is used. All cases have been modelled in the steady state condition, using a mixing plane interface between rotor and stator frames. The isometric view of a single passage computational domain is demonstrated in Fig. 6.

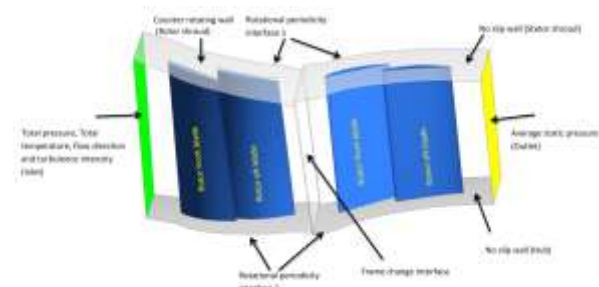


**Fig. 6.** Isometric view of the reference single passage and Boundary conditions.

### Validation of the numerical method

The performance of NASA Rotor and Stage 37 has been simulated to validate the developed numerical model. Geometrical parameters, blade point coordinates and stage characteristic maps are reported in [14]. The isolated rotor characteristic map experimental results are also reported in [15]. In order to validate the current numerical model, the 3D flow through the Rotor and Stage 37 in rotational design speed has been numerically modelled with the structured H-type grid, and the results are presented and compared.

Prior to comparing the results obtained from the simulation and the reported data mentioned above, a grid sensitivity analysis was completed for the Stage 37 case. The computational domain was

discretized by using a structured H-type grid in the passages and an O-type grid in the boundary layer regions for more accurate results. Three sets are compared with each other to study the independency of results from the number of nodes in the generated computational grids. Some information about these sets is presented in Table 4, and a close view of the rotor computational grid is depicted at the mid-span height in Fig. 7.

**Table 4.** Computational grid specifications for Stage 37

Grid	No. of Nodes	No. of Layers throughout the Blades' Height
Coarse r,s	60k, 40k	30
Medium r,s	270k, 200k	50
Fine r,s	450k, 350k	80

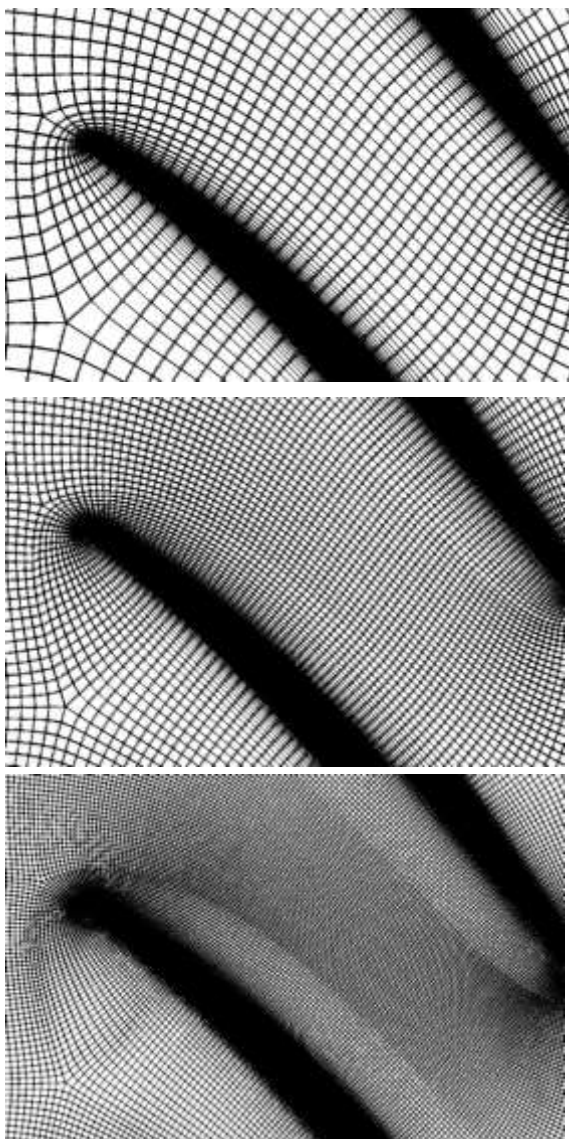


**Fig. 7.** Mid-span layer of Rotor 37 computational coarse, medium and fine grids.

In the case of Stage 37, the computations were done at the near-peak efficiency point of the design speed, which is 17188.7 RPM. At the design point, this stage delivers a pressure ratio of 2.05 at the mass flow rate of 20.54 kg/s. The three-dimensional flow is analyzed under this condition using the mentioned sets of computational grids, and the results have been reported in Table 5.

**Table 5.** Grid study results for Stage 37.

Grid	Mass flow Rate (kg/s)	$\pi$	%Difference in Mass flow rate	%Difference in $\pi$
Coarse	20.243	2.0534	-	-
Medium	20.537	2.0575	1.4535	0.2033
Fine	20.541	2.0576	0.0182	0.0012

As indicated in Table 5, the difference between the first and second sets of grids is approximately 1.45% in terms of mass flow rate, and the similar difference between the second and third sets of grids is approximately 0.018%. Complete analysis of other flow parameters among these three sets proved that the medium case provides sufficient accuracy, and thus from this point on, this set would be used to continue this study.

In the published Fig. 8, the experimental results and current computational results of the isolated rotor and stage characteristic maps are demonstrated and compared. As mentioned before, experimental rotor values were taken from [15] and the experimental stage results were taken from [14].

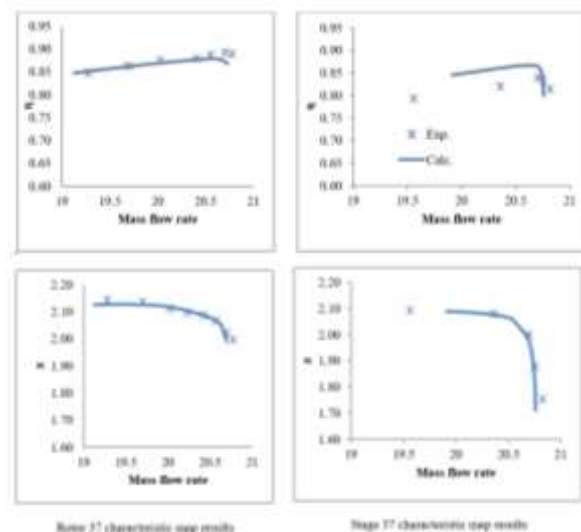


**Fig. 8** Comparison of the reported experiments and current numerical simulations for the Stage and Rotor 37 characteristic maps

In the case of Rotor 37, the maximum relative error in  $\eta$  and  $\pi$  is less than 0.8%. The current numerical method predicts a lower  $\eta$  value in the peak efficiency point. However, for the whole stage, the maximum relative errors in terms of  $\eta$  and  $\pi$  are approximately 3% and 0.2%, respectively. Moreover, the numerical studies here predict higher efficiency values for Stage 37 compared to the experimental reports. The choking mass flow rate is also compared; the relative error in maximum mass flow rate in Stage 37 is about 0.3% while it is less than 0.17% for the rotor case. In both cases, the numerical mass flow is less than the experimental reported one. Authors believe that additional details on the validation case, especially on Stage 37, may help to obtain a more accurate model and decrease the relative errors. For example, the authors have just the tip clearance value, and simply truncated the tip region of Rotor 37. Given the high blade velocities in this region, the non-accurate geometrical model may result in significant deviations from the experimental case. It must be added that the numerical model under predicts Stage 37 stall margin, The obtained mass flow rate of the surge point from the computational studies is 19.908 kg/s while the reported experimental one is 19.56 kg/s. Thus, it is believed that using a more accurate computational frame change model improves the accuracy of this validation.

In order to complete the validation process, relative Mach number contours of the isolated rotor are presented and compared. In order to validate the rotor near stall condition, relative Mach number contours have been compared in the 95% span. In this region, tip leakage vortices will appear and more complicated flow pattern must be detected. The comparison is depicted in Fig. 9 between the current numerical results and the experimental results [15].

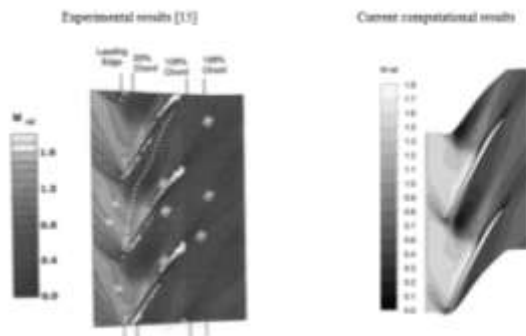


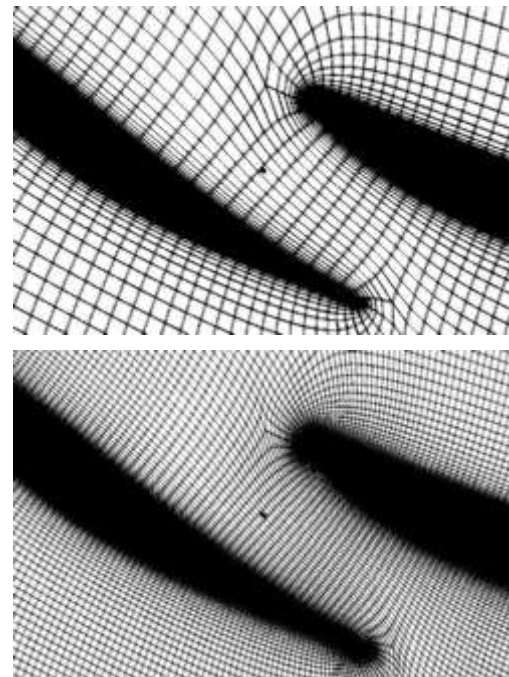
**Fig. 9.** Mach number contours comparison for the 95% span, the near stall condition of rotor 37.

The current comparison also shows good agreement in flow field identification, the shock structure, shock-boundary layer interaction, separated region, trailing edge wakes and after-shock diffusion in the tip region. The same numerical model will be used for the remaining part of the research. Similarly, a grid sensitivity analysis was done for the understudied tandem case. Due to the large number of cases, this analysis was only performed for the peak efficiency point of the reference case (which doesn't have any solidity deviation). Three sets of computational grids are mentioned in Table 6.

**Table 6.** Computational grid specifications of the tandem reference case.

Grid	Number of Nodes	No. of Layers throughout the Blade's Height
Coarse r,s	200k,150k	30
Medium r,s	600k,550k	50
Fine r,s	1800k,1600k	80

In these sets of grids, H-type grid is used in passages and O-type grid around the blades. The mid-span views of these sets are presented in Fig. 10.



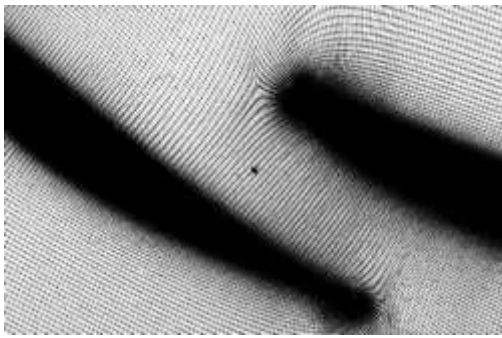


**Fig. 10.** Mid-Span view of the tandem computational coarse, medium and fine grids

The flow structure is more complicated in the tandem case; the higher Number of blades results in more stagnation points and broader areas of complex flows around the leading and the trailing edges. Moreover, the interaction of the boundary layer of the front and aft blades must be taken into consideration as a challenging phenomenon. Thus, the computational set of grids for the tandem case includes more nodes than the one used for the conventional case. Table 7 indicates the grid study results and a briefed comparison of grid refinement, for the reference case and the near peak efficiency point.

**Table 7.** Grid study results for the tandem case

Grid	Mass flow Rate (kg/s)	$\pi$	%Differen ce in Mass flow rate	%Differen ce in $\pi$
Coarse	42.75	1.241	-	-
	3	2		
Mediu m	43.38	1.245	1.4806	0.3222
	6	2		
Fine	43.72	1.247	0.7836	0.1847
	6	5		

Obviously, the difference between the coarse and the medium cases is less than 1.5%, and the difference between the medium and the fine cases is less than 0.8%, which is insignificant.

### Results and discussion

As mentioned earlier in Table 3, seven cases will be compared to the reference one. Results associated with solidity deviation of -21% to +55% from the original case are plotted in the following figures as well as the ones associated with -34% case. However, as the results of this last case do

not follow the patterns observed in other cases, they would not be taken into consideration when forming conclusions. This will be discussed in more details later.

Fig. 11 demonstrates the stage efficiency of the system versus the flow coefficient in different operating points of each of the nine cases. As depicted, when solidity increases from -21% to 55%, the peak efficiency of the system in the corresponding case shifts to the lower flow coefficients part which is at the left of this figure

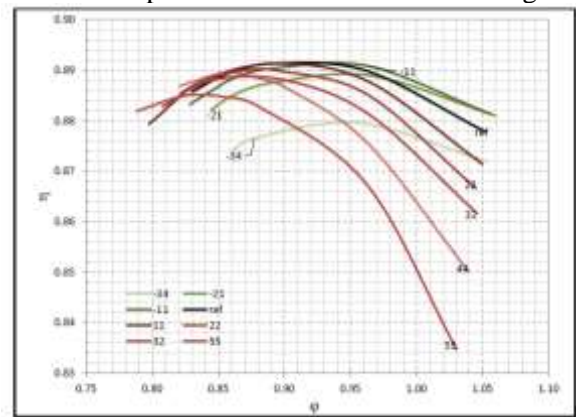


**Fig. 11.** Stage efficiency vs. the flow coefficient

The flow coefficient corresponding to the peak efficiency of -21% occurs at 0.956, while the same quantity for the 55% case occurs at a flow coefficient of 0.825. Another noticeable point is that as the solidity deviation increases, the flow coefficient and efficiency corresponding to the maximum inlet mass flow rate decrease. For example, at -21%, the maximum inlet mass flow rate occurs at a flow coefficient of 1.06 and shows an efficiency of 0.881. In comparison, the same parameter at +55% occurs at a flow coefficient of 1.03 and shows an efficiency of 0.835. As represented, the associated results with -34% don't follow these mentioned patterns, and it also shows a poor performance compared to all other cases. This poor performance may be the result of a low number of blades which decreases the capability of the system to direct the flow inside the machine. Thus, this case will not be regarded in forming the conclusions of this study. Summarized data in the other eight cases are presented in Table 8.

**Table 8.** Summarized data in different cases

Solidity Value Deviation (%)	Max. $\eta$	$\phi$ in Max. $\eta$	Mass Flow in Max. $\eta$ (kg/s)	$\eta$ in Max Mass Flow	Max. Mass Flow (kg/s)
-21	0.8889	0.9645	46.3085	0.8810	49.8061
-11	0.8908	0.9631	46.2640	0.8814	49.6977
0	0.8913	0.8909	43.4305	0.8778	49.5442
11	0.8912	0.8955	43.6189	0.8714	49.4685
22	0.8900	0.8694	42.5615	0.8666	49.3062
32	0.8881	0.8995	43.7831	0.8617	49.3144
44	0.8895	0.8539	41.9270	0.8501	49.0961
55	0.8850	0.8247	40.7101	0.8346	48.7849

Fig. 12 demonstrates the maximum efficiency of each case versus the solidity deviation. As represented, the highest efficiency value occurs in the reference solidity, which is chosen using the suggested procedure in part III. The used correlation is derived considering minimizing the profile and secondary flow losses. This criterion confirms the suggested guideline for the solidity selection strategy in the current tandem-bladed design.

For the other cases, the system performance deteriorates as solidity values deviate from the reference quantity. This deterioration is more significant and observable as it proceeded to large negative values such as -34%. According to the results presented here, the last point on the negative side of this diagram, which follows the mentioned patterns in Fig. 11, must lie somewhere between -21% and -34%. On the other side, increasing solidity values to more than 55% has a similar deteriorating effect on the performance. Fig. 11 also shows that increasing the solidity value, results in blockage of the flow, which has a significant negative effect on the performance. This fact can be better understood by looking at the last column of Table 8.

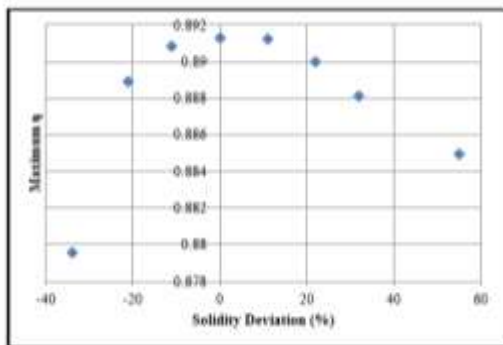


**Fig. 12.** Efficiency vs. solidity deviation.

In order to investigate the effect of solidity on aerodynamic loading of the current case, Fig. 13 is presented, which shows the characteristic curves of  $\psi$  versus  $\phi$ , and shows that solidity deviations affect  $\psi$ - $\phi$  characteristic curves and, therefore it should be taken into consideration when analyzing the performance.

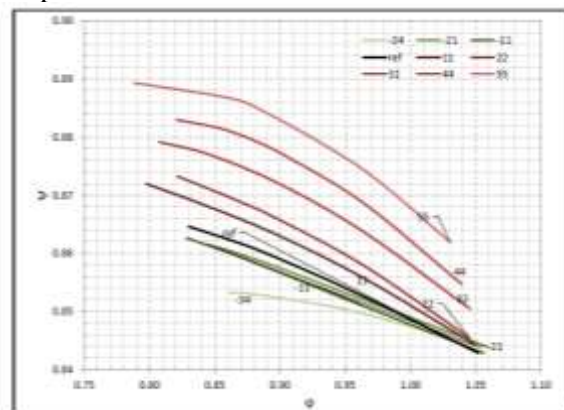


**Fig. 13.** Characteristic curve of  $\psi$ - $\phi$

Here, two phenomena are discoverable. The first is work coefficient shifting up due to the solidity increase, which is because of better flow guidance and improved adherence of the flow over the profile suction sides in a higher number of blade cases. The other, is the decrease in flow coefficients in higher solid cases which shifts the characteristic curves to the left. In higher solidity values, the integral of occupied volume by the momentum thickness in the compressor passage increases. This reduces the average passing velocity and the average flow coefficient, depicted in the curves' left shift.

Likewise, by the solidity increase, absolute magnitudes of the corresponding characteristic curve's slopes increase too. To illustrate this point better, Fig. 14 is presented. It depicts that increasing the magnitude of the curve's slope

shows a linear behavior with an increase of the solidity deviation. For example, the slope's magnitude in -21% is 0.0857 while it is 0.187 in the 55% case which shows a more than 118% increase. The interesting point is that although the curves' slopes experience such a large change, a similar change is not observed in the magnitude of  $\psi$  at constant  $\phi$ , this means that while the solidity deviation increases largely,  $\psi$  values do not show a similar pattern. For example, at a flow coefficient of 0.92, as proceeded from -21% to +55%,  $\psi$  values increase from 0.856 to 0.88 which shows less than 3% improvement in  $\psi$  over 77% increase in the solidity deviation. Thus, gaining higher  $\psi$  values cannot be a good motivation to increase solidity in this system.

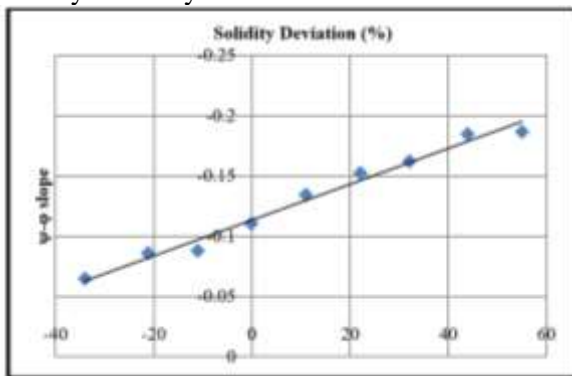


Fig. 14.  $\psi$ - $\phi$  Characteristic curve slope vs. solidity deviation.

Considering the isentropic relation, the pressure ratio value is a function of several parameters such as efficiency, work coefficient, total inlet temperature and rotational speed of the system. In the current numerical analyses, all cases have the same rotational speeds as well as similar inlet conditions. Thus, the pressure ratio of all cases can be determined mostly with the parameters  $\psi$  and  $\eta$ . Fig. 15 depicts the multiplication of these two parameters versus the  $\phi$ . Some interesting facts can be observed. At first, it is indicated that all curves except the one corresponding to -34% seem to have a common point with each other. This point occurs approximately in the flow coefficient of 0.963. Thus, in case flow coefficients near this value are of interest, solidity seems not to have a significant effect on the obtained pressure ratio of the system.

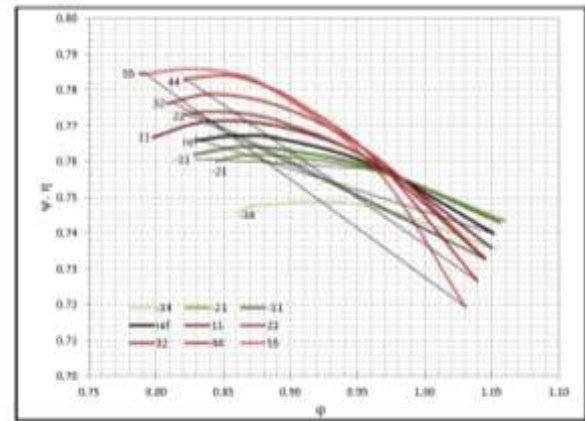
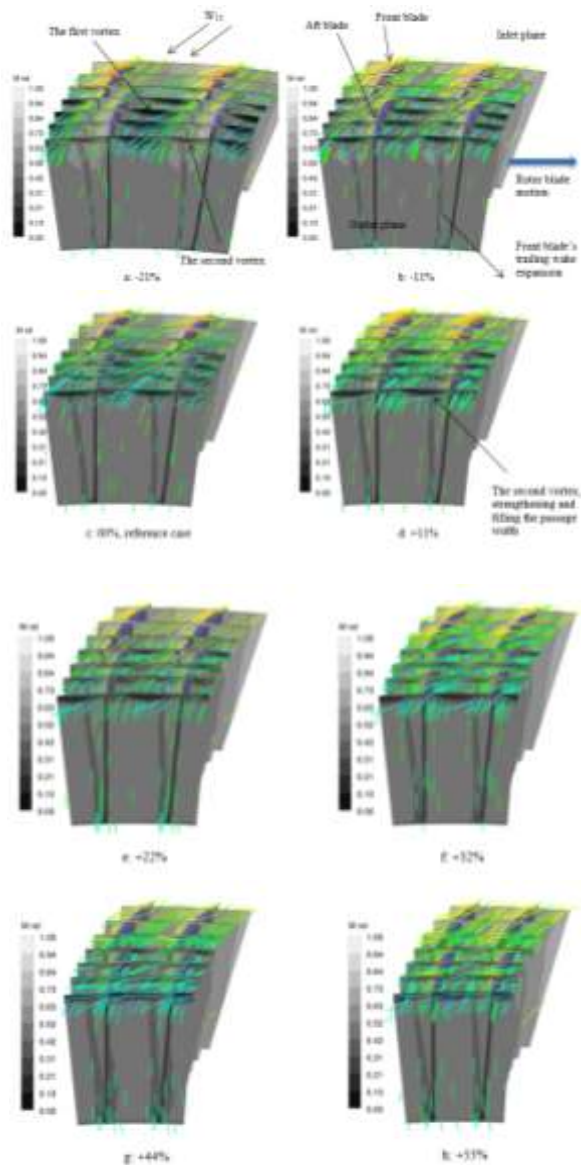


Fig. 15. Multiplication of  $\psi$  to  $\eta$  vs.  $\phi$ .

On the right side of this figure, while the solidity deviation increases, the last points of the corresponding curve would gain a lower quantity. This is a direct result of the pattern discussed in Fig. 12. There; it was mentioned that at the maximum inlet mass flow rate of each case, as solidity deviation increases, lower efficiency values would be obtained. These lower efficiency values affect this multiplication; therefore, on the right side of Fig. 15, a similar pattern to Fig. 11 is observed. However, an opposite trend is observed on the left side of this figure. The reason is that on the stall side of the characteristic, there is no major difference in  $\eta$  of different cases, as previously observed in Fig. 11. However, as depicted in Figs. 13 & 14, as the solidity deviation increases, the work coefficient values increase correspondingly. Thus, the last point on the left side would have higher values of this multiplication when the solidity deviation increases. Because of the direct relation between the pressure ratio and the multiplication of  $\psi$  to  $\eta$ , a similar behavior will occur in the pressure ratio-mass flow curve.

In order to investigate the effect of solidity deviation on the tandem rotor passage flow fields, relative Mach number contours have been plotted in several planes from hub to tip sections in Fig. 16. The plots have been oriented as a view from above the rotor so that the blade boundary layer wake and its effect on the tip leakage flow can be detected. All contours have been provided in the peak efficiency point for the corresponding case. The tip leakage flow stream lines have also been added to the Mach number contours.



**Fig. 16.** Inlet to outlet flow field, from Upper view Mach number contours, with tip leakage flow vortices through the tandem passage with different solidity conditions.

Generally, it is observed that the larger portion of the tip vortex originates from the trailing edge of the front blade due to the high pressure gradient between the suction and the pressure surfaces of this blade. This vortex continues over the aft blade pressure side. In low solidity cases, especially -21%, -11% and the reference case, another vortex is detected over the aft blade's suction surface, originating from the aft blade pressure gradient in the tip region. As solidity deviation increases, this second vortex gets stronger while the first one gets weaker. This pattern continues to the extent that in higher solidity deviations, the only detected vortex

is the second one which fills the passage tip at the rotor outlet. In these cases, although the first vortex still occurs, it mixes with the second vortex before the rotor's outlet, so it cannot be detected separately.

Furthermore, it is seen that the wake originating from the front blade trailing edge continues throughout the passage. This wake imposes extreme non-uniformity in the flow pattern at the rotor outlet. Likewise, it encounters the aft blade trailing edge wake at the hub corner in high solidity cases; however, in -21%, -11% and ref. cases, it has enough space to form a separate way throughout the passage. It must be mentioned that the front blade trailing edge wake expands circumferentially through the machine axis. It forms a low momentum region in the flow passage, making a virtual cavity over the aft blade suction surface. In the current study, it is desired to focus on the effect of this low momentum region on the rotor tip leakage vortices.

Increasing the solidity results in lower average Mach numbers (distributed over the blade's outlet), which is because of the decrease in the mass flow rate. In low solidity cases, local high-speed regions can be detected in above 80% of span, decreasing in magnitude and covered area as solidity deviation increases. Thus, these regions do not form in cases other than -21% and -11%. High-speed regions in low-solidity cases affect the wake at this section and therefore neutralize the mentioned cavity locally. In other cases, the only non-uniform phenomenon is the front blade trailing edge wake.

## Conclusion

This analysis showed that the decided strategy identifies the optimal value for solidity or number of blades, which leads to finding the case with the maximum efficiency; consequently, the maximum efficiency of the reference case would be higher than all other cases. However, it was observed that up to  $\pm 20\%$  deviations of solidity from the reference case do not change the maximum efficiency value significantly. Solidity deviation not only changes the compressor's maximum efficiency but also affects the work coefficient vs. flow coefficient behavior and the compressor characteristic maps. The solidity deviation enormously influences the  $\psi$ - $\phi$  curve slope so that a 55% increase in the reference solidity value faces the  $\psi$ - $\phi$  curve slope to about 68% increase. This

shows that solidity selection can be used as a tool to shape the characteristic map of a tandem-bladed compressor.

Compressor characteristic maps were derived from the mass-averaged properties of inlet and outlet conditions; however, many phenomena in the flow field need 3D flow analysis to be understood. The current study also investigated the effect of solidity deviation on the tip leakage flow pattern. The complexity of tip vortices structure in tandem cases was shown and discussed, and the formation of the trailing edge wakes by the passage width was analyzed.

In conducting this analysis, it was decided to concentrate mainly on the effect of solidity deviation. Therefore, very few changes were applied to the parameters in other cases. In future studies on this subject, the effect of different blade thicknesses on performance can be analyzed. It is anticipated that this future study results in choosing the thinnest possible airfoil section to increase the possible flow passage. However, in that case, structural problems may arise that need relevant analyses.

## References

- [1] Cheatham, JG., "Single-stage experimental evaluation of tandem-airfoil rotor and stator blading for compressors. Part VII: Data and performance for stage E," NASA Lewis Research Center, NASA CR-134529, 1974.
- [2] Brent, JA., and Clemmons, DR., "Single-stage experimental evaluation of tandem-airfoil rotor and stator blading for compressors. Part VIII: Final report," NASA Lewis Research Center, NASA CR-134713, 1975.
- [3] Bammert, K. and Beelte, H., "Investigations of an axial flow compressor with tandem cascades," *Engineering for Gas Turbines and Power*, Vol. 102, No. 4, 1980, pp.971-978. doi:10.1115/1.3230369
- [4] McGlumphy, J., Wellborn, SR., Kempf, S., and Ng W-F., "Numerical Investigation of Tandem Airfoils for Subsonic Axial-Flow Compressor Blades," *Turbomachinery*, Vol. 131, No. 2, 2009, pp.021018. doi:10.1115/1.2952366
- [5] McGlumphy, J., Wellborn, SR., Kempf, S., and Ng W-F., "3D numerical investigation of tandem airfoils for a core compressor rotor," *Turbomachinery*, Vol. 132, No. 3, 2010, pp.031009. doi:10.1115/1.3149283
- [6] Qiushi, L., Hong, W., and Sheng, Z., "Application of tandem cascade to design of fan stator with supersonic inflow," *Chinese Journal of Aeronautics*, Vol. 23, No. 1, 2010, pp.9-14. doi: 10.1016/S1000-9361(09)60181-3
- [7] Shen, C., Qiang, X., and Teng, J., "Numerical and experimental investigation of an axial compressor flow with tandem cascade," *Thermal Science*, Vol. 21, No. 6, 2012, pp.500-8. doi: 10.1007/s11630-012-0574-x
- [8] Eshraghi, H., Boroomand, M., and Tousi, A.M., "Design and Analysis of a Highly Loaded Tandem Compressor Stage," *ASME 2014 International Mechanical Engineering Congress and Exposition*, Montreal, Quebec, Canada, 2014, pp. V001T01A071. doi:10.1115/IMECE2014-39750
- [9] M. Mohsen, F. M. Owis, A. A. Hashim, "The impact of tandem rotor blades on the performance of transonic axial compressors," *Aerospace Science and Technology*, Vol. 67, 2017, pp. 237-248. doi: 10.1016/j.ast.2017.04.019
- [10] Yue S, Wang Y, Wang H. "Design and optimization of tandem arranged cascade in a transonic compressor," *Journal of Thermal Science*, Vol. 27, No. 4, 2018, pp.349-358. doi: 10.1007/s11630-018-1013-4
- [11] Song Z, Liu B. "Optimization design for tandem cascades of compressors based on adaptive particle swarm optimization," *Engineering Applications of Computational Fluid Mechanics*, Vol. 12, No. 1, 2018, pp.535-552. doi: 10.1080/19942060.2018.1474806
- [12] Yang Z, Liu B, Mao X, Zhang B, Wang H. "Research on the Influence of Inflow Conditions on the Aerodynamic Performance of a Tandem Cascade," *Journal of Applied Fluid Mechanics*, Vol 15. No. 6, 2022, pp.1745-1758. doi: 10.47176/jafm.15.06.1206
- [13] Tournier, J.M., El-Genk, MS., "Axial flow, multi-stage turbine and compressor models," *Energy Conversion and Management*, Vol. 51, No. 1, 2010, pp.16-29. doi:10.1016/j.enconman.2009.08.005
- [14] Reid, L., and Moore, R.D., "Design and Overall Performance of Four Highly Loaded, High-Speed Inlet Stages for an advanced High-Pressure-Ratio Core Compressor," NASA Lewis Research Center, NASA Technical Paper 1337, 1978.
- [15] Suder, K. L., "Experimental investigation of the flow field in a transonic, axial flow compressor with respect to the development of blockage and loss," NASA Lewis Research Center, NASA Technical Memorandum 107310, 1996.

## COPYRIGHTS

©2022 by the authors. Published by Iranian Aerospace Society This article is an open access article distributed under the terms and conditions of the Creative Commons Attribution 4.0 International (CC BY 4.0)

(<https://creativecommons.org/licenses/by/4.0/>).

